Geometric Positioning Accuracy Improvement Method of Micro SAR Satellites With Large Positioning Errors

Qian Cheng , Taoyang Wang , Xin Li , Yongcheng Wan, and Maoqiang Jing

Abstract—The rapid development of micro synthetic aperture radar (SAR) satellites provides a new means of all-day, all-weather, and high-frequency Earth observation. However, the geometric stability of micro SAR satellites is weak, and the geometric positioning error of SAR images is large. The traditional method improves the geometric positioning accuracy (GPA) of satellite images by adding well-distributed ground control points (GCPs), but it is time-consuming and laborious. This study proposed a method for improving the GPA of micro SAR satellites with large positioning errors. The proposed method designs a multilevel and multiscale SAR image matching framework, utilizes high-precision spaceborne SAR digital orthophoto image (DOM), and realizes high-precision virtual GCPs (VGCPs) extraction between micro SAR satellite images and DOM through image matching. Finally, using the matched VGCPs directly participate in the geometric correction to improve the GPA of the micro SAR images. The experiment adopted Gaofen-3 (GF-3) 10-m resolution DOM product as the control data. VGCPs were extracted and GPA was evaluated for five Luojia-2 (LJ-2) SAR images (3-m resolution, stripmap mode). The results show that the GPA of the LJ-2 image is at the kilometer level, and it can be improved to better than 5 m (relative to GF-3 DOM) after processing, which proves the validity and reliability of the proposed method. The proposed method can provide support for the cooperative processing of multisource SAR satellite images.

Index Terms—Geometric positioning accuracy (GPA), image matching, Luojia-2 (LJ-2), micro SAR satellite.

NOMENCLATURE

Abbreviations and Acronyms

SAR	Synthetic aperture radar.
GPA	Geometric positioning accuracy.
LPE	Large positioning error.
GCPs	Ground control points.
DOM	Digital orthophoto image.
VGCPs	Virtual GCPs.
GF-3	Gaofen-3.
LJ-2	Luojia-2.
VGCPMF	VGCPs matching framework.
RFM	Rational function model.
BA	Block adjustment.
NCM	Number of correct matches.

I. INTRODUCTION

IN RECENT years, large and medium-sized synthetic aperture radar (SAR) satellites (standard SAR satellites) have continued to develop in the direction of high-resolution, wide-width, multiorbit, and multidimensional. At the same time, micro SAR satellites, with the characteristics of "single star low cost, constellation high revisit," have good application prospects in commercial, emergency, and military fields and have become a research hotspot. For example, ICEYE [1] and Capella [2] series satellites. Data from microsatellites (e.g., optical or SAR microsatellite) has a relatively poor geometric positioning accuracy (GPA) compared to the data from medium-sized standard satellites. The low mass and volume of microsatellites limit their orbit accuracy and also limit their instrumentation (e.g., w.r.t. high precision GNSS receivers). Therefore, the GPA of microsatellites is unstable, usually ranging from tens of meters to a few kilometers [3]. The poor GPA of microsatellites questions and even prevents the usability of their data for many use cases.

The geometric orientation of satellite images is a fundamental step in photogrammetry, and traditional methods rely on a certain number of well-distributed ground control points (GCPs). However, the acquisition of GCPs is time-consuming and laborious [3]. To improve the GPA, using other control data to replace GCPs, such as high-precision digital orthophoto image (DOM), digital surface model, and laser point product [4], [5]. In addition, some scholars conduct joint processing of optical and SAR images to obtain high-precision orientation results [6], [7], but there are few reports on the joint processing of multisource SAR images. To improve the GPA of micro SAR satellites, the standard SAR satellites (e.g., GF-3) with high measurement accuracy can be selected as the reference for joint processing based on the idea of joint processing of optical and SAR images.

Fig. 1 shows the uniqueness of the Luojia-2 (LJ-2) Ka SAR image, where the green area is the heavy rainfall area, which can be used for rainstorm and flood monitoring. LJ-2 is a Ka-band SAR satellite jointly developed by Wuhan University and China Academy of Space Technology, with a mass of less than 360 kg,
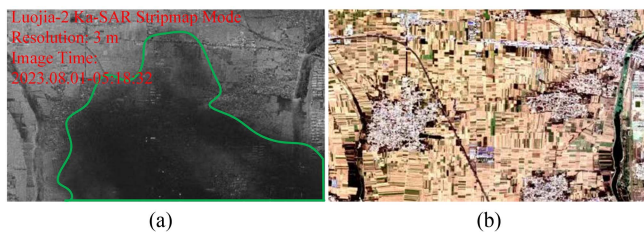
Fig. 1.   Comparison of Luojia-2 Ka SAR and optical images. (a) Luojia-2 Image. (b) Optical Image.

belonging to the category of the microsatellite. The satellite has stripmap, sliding-spot, and video modes. It can obtain Ka-band SAR images with a maximum resolution of 1 m, which can be applied to marine environment monitoring and flood detection. LJ-2 is limited by the satellite size, and the platform stability is difficult to ensure. As a result, the satellite's initial positioning accuracy is poor, limiting its fine application in the industry. Standard SAR satellites can provide high-precision data for multi-industry users. For example, the positioning accuracy of Chinese C-band Gaofen-3 (GF-3) can be better than 3 m after geometric calibration [8]. To quickly promote micro SAR satellites to industrial applications, this study proposes a method to improve the GPA of micro SAR images for large positioning error (LPE). The GF-3 SAR DOM product is used as the control data, and the LJ-2 SAR image positioning accuracy is improved by matching the high-precision virtual GCPs (VGCPs).

The main contributions of this study include the following three aspects.

1) A multilevel and multiscale SAR image matching framework is proposed to support high-precision VGCPs extraction from RFM images with LPE and DOM, named VGCPs matching framework (VGCPMF).
2) Aiming at the differences between Ka-SAR and C-SAR, 10 matching algorithms are used to conduct multigroup matching experiments, and RIFT is selected for multisource SAR matching while taking into account LPEs.
3) Based on the GF-3 SAR DOM, the image accuracy of five LJ-2 images (stripmap mode) was verified and improved, the initial GPA of kilometer level was improved to better than 5 m.

II. RELATED WORK

In the application of remote sensing satellite images, the GPA of the images is a key index to measure the quality of remote sensing data. To improve the GPA of satellite images, a large number of relevant studies have been carried out [9]. For satellite images with poor positioning accuracy, the traditional method can be used to improve the GPA by adding well-distributed GCPs, but it is time-consuming and laborious. With the development of block adjustment (BA) based on sparse control conditions, it is no longer necessary to set GCPs for each image, which reduces the demand for the number of GCPs [10]. In addition to GCPs, other control conditions, such as linear control conditions (roads, water systems, etc.) have also been tried to be introduced into the BA for optical stereo images [11].

In recent years, with the increase in the variety of public geographic data and the improvement of positioning accuracy, the use of geographic data for BA has become an effective method. These public geographic data, including DOM and digital elevation model (DEM), etc., have higher GPA compared with the original satellite images. Utilizing these as control data, satellite image positioning accuracy can be improved even without GCPs. In addition, some scholars directly use SRTM-DEM as ground control [12]. This method allows the existing DEM to be used for BA of optical stereo images, with the advantage of not needing to obtain external GCPs. However, the public geographic data will have the problem of geographic offset, or information hiding can not be avoided, and it is difficult to apply in some areas.

In addition to the use of control data or virtual control data to improve the GPA of satellite images, the BA of optical satellite stereo pairs without GCPs has gradually attracted attention. There is a certain degree of residual random errors in optical satellite images, and these errors have a certain degree of randomness for satellite images with different times and orbits. As a result, the random errors of the tie points between different stereo pairs can be reduced when calculating the spatial coordinates, and the positioning accuracy without GCPs after BA is usually better than that of the original stereo pairs [13], [14]. Another approach to improve the accuracy is to include some commercial satellite images (e.g., GeoEye and WorldView, etc.) with higher positioning accuracy in the study area for the joint BA of multisource satellite images [15]. This method of utilizing information redundancy to eliminate the error requires multiview images, which cannot be applied to single-view images.

In addition to using multisource data to improve the positioning accuracy of remote sensing satellite images, geometric calibration can also be used to realize it. Spaceborne SAR geometric calibration is to find out the main error sources and calibrate the errors to improve the GPA [16]. Standard SAR satellite adopts geometric calibration methods and can obtain meter-level results. Research results show that COSMOSky-Med stripmap, sliding-spot modes planimetric positioning accuracy reaches 3 m and 1 m respectively [17]; For TerraSAR-X satellite, the absolute positioning accuracy is 0.5 m in azimuth direction and 0.3 m in range direction [18]; Yaogan-13 stripmap and sliding-spot modes planimetric positioning accuracy can reach better than 3 m and 1.5 m, respectively [19], [20]; The GPA of GF-3 satellite is better than 3 m [8].

In the existing multisource satellite image processing, the focus is on the improvement of positioning accuracy of optical satellites, and there is little mention of the research on micro SAR satellites. In addition, although geometric calibration can achieve high GPA, it requires the satellite to maintain a stable state for some time, at which time the parameters of geometric calibration can effectively compensate for the system error. However, the unstable attitude and large number of microsatellites in orbit make it difficult to use the geometric calibration method effectively. With the rapid development of micro SAR satellites, it is an unavoidable problem to improve the GPA of micro SAR satellites quickly and effectively.

III. METHOD

Micro SAR satellite positioning errors range from tens of meters to several kilometers, and this uncertainty poses a great challenge to the matching between satellite images and DOM. This study proposes a method to improve the positioning accuracy of micro SAR satellite images, which can realize high-precision matching of micro SAR satellite images with DOM and VGCPs extraction. The method mainly consists of following three parts:

1) adaptive matching pair acquisition;
2) image match;
3) VGCPs generation and gross error elimination.

A. Adaptive Matching Pair Acquisition

1) Image Cell Step Calculation: Set the number of cells in the column and row directions to nGX and nGY, respectively, and the image cell step can be calculated by

$$\begin{cases} \Delta gX = \text{Width}/\left(nGX + 1\right) \\ \Delta gY = \text{Height}/\left(nGY + 1\right) \end{cases} \quad (1)$$

where ΔgX and ΔgY are cell steps in the column and row directions, respectively. Here, the way of rounding (/) adopts the floor method.

2) Image Cell Construction: Four corners (pixel coordinate) of the image cell are calculated as follows:

$$\begin{cases} \text{CEL}_{i,j}^{LT} \left(i \cdot \Delta gX - Ker/2, j \cdot \Delta gY - Ker/2\right) \\ \text{CEL}_{i,j}^{RT} \left(i \cdot \Delta gX + Ker/2, j \cdot \Delta gY - Ker/2\right) \\ \text{CEL}_{i,j}^{RB} \left(i \cdot \Delta gX + Ker/2, j \cdot \Delta gY + Ker/2\right) \\ \text{CEL}_{i,j}^{LB} \left(i \cdot \Delta gX - Ker/2, j \cdot \Delta gY + Ker/2\right) \end{cases} \quad (2)$$

where $i \in [1, nGX], j \in [1, nGY]$. *Ker* is image cell size, it can be set by the user. In this study, *Ker* is set to 2048 and 1024 in *L0* and *Li* matching phase, respectively. $\text{CEL}_{i,j}^{LT}$, $\text{CEL}_{i,j}^{RT}$, $\text{CEL}_{i,j}^{RB}$, and $\text{CEL}_{i,j}^{LB}$ are the *i*th column and the *j*th row image cell's four corners, respectively.

3) Ground Cell Generation: The four corners combined with the positioning model (rational function model (RFM) in this study) and DEM data can be mapped into geodetic coordinates. The minimum enclosing rectangle of the geodetic coordinates is used as the ground cell.

4) Local Geometric Correction and Resampling: The SAR image is corrected according to the ground cell to obtain the geometry correction cell, DOM cell is resampled according to the ground cell to obtain the DOM cell. Therefore, geometry correction cells and DOM cells form matching pairs. The sampling resolution is the original SAR resolution multiplied by the resolution threshold (denotes Tres). The original SAR image resolution can be obtained by projecting two image points onto the ground and calculating the ratio of the ground distance to the image distance [21]. Fig. 2 is the schematic of pair acquisition.

B. Image Match

The matching pairs acquired in Section III-A are corrected, at which point rotation and scale differences are reduced [21]. It should be noted that the correction operation cannot reduce
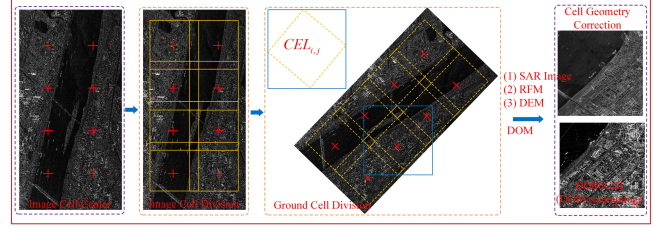

Fig. 2. Schematic of pair acquisition.

the translational motion between the original images. In addition, the acquired matching pairs convert large remote sensing images into image slices of appropriate size. Therefore, the state-of-the-art (SOTA) matching algorithms can be directly used without any improvement. The matching methods may include intensity-based methods, feature-based methods, and learning-based methods.

C. VGCPs Generation and Gross Error Elimination

The initial matching points of the whole image can be obtained by merging the matching points of each cell, and the relationship is as follows.

1) VGCPs Generation: The homonymous points in the image-matching phase are the image coordinates of the cell and cannot be directly corrected for RFM. Therefore, postprocessing of the matching results is required.

Step 1, Geometry correction cell points conversion. Points on the geometry correction cell are first turned into latitude and longitude coordinates based on geographic relationships, and then the elevations are interpolated from the DEM to form 3D geodetic coordinates. Finally, the RFM inversion method is used to map the 3D geodetic coordinates to the pixel coordinates on the whole SAR, as the pixel coordinates of the VGCPs. The interpolation method here is consistent with the way the elevation is interpolated on the DEM during geometry correction. This approach ensures that the elevation values are the same at the same latitude and longitude. Details of the conversion process can be found in our previous work [21].

Step 2, DOM cell points conversion. Points on the DOM cell are turned into latitude and longitude coordinates based on geographic relationships, and then the elevations are interpolated from the DEM to form 3D geodetic coordinates, as geodetic coordinates of the VGCPs.

2) Gross Error Elimination: The recovered VGCPs are derived from the geometry correction and DOM cells, which inevitably have mismatched points. Therefore, it is necessary to eliminate the mismatched points from the global perspective. Considering the large size characteristics of remote sensing images, it is difficult to fit all points effectively by using simple geometric transformation models such as polynomial and affine transformation [21]. This study proposes an iterative mismatched point elimination method based on single-view image bundle adjustment to realize VGCPs gross error elimination. The systematic error compensation model in the image space is used to compensate for the systematic error of the RFM of SAR

image [22], which can be described as

$$\begin{cases} l = \frac{N_l(X,Y,Z)}{D_l(X,Y,Z)} + e_0 + e_1 l + e_2 s \\ s = \frac{N_s(X,Y,Z)}{D_s(X,Y,Z)} + f_0 + f_1 l + f_2 s \end{cases} \quad (3)$$

where (l, s) is image point coordinates (R, C) after regularization, (X, Y, Z) is 3D geodetic coordinates (U, V, W) after regularization. N_l, D_l, N_s, and D_s are a cubic polynomial functions containing (X, Y, Z). $(e_0, e_1, e_2, f_0, f_1, f_2)$ is affine transformation parameters for the systematic error compensation model.

In traditional BA, the tie points and the GCPs exist simultaneously. In this study, only single-image is processed, not multiview images, i.e., there is no tie point and its corresponding encryption point in the BA system. Therefore, the BA model is simplified into a single-image BA model.

In (3), l and s can be represented by (X, Y, Z) and $\boldsymbol{t} = (e_0, e_1, e_2, f_0, f_1, f_2)^T$, i.e., the RFM model of a single image can be represented as $l = g^l(X, Y, Z, \boldsymbol{t})$ (marked g^l) and $s = g^s(X, Y, Z, \boldsymbol{t})$ (marked g^s). Denote (X^k, Y^k, Z^k) and (l^k, s^k) as the 3D geodetic coordinates and image point coordinates of the kth GCP. ξ^k denotes the weight of the kth GCPs. Then the BA model can be transformed into a solving optimization problem that

$$\boldsymbol{t} = \arg\min(Q) \quad (4)$$

$$Q = \sum_{k=1}^{K} \xi^k \left\{ \left[g_k^l \left(X^k, Y^k, Z^k, \boldsymbol{t} \right) - l^k \right]^2 \right.$$
$$\left. + \left[g_k^s \left(X^k, Y^k, Z^k, \boldsymbol{t} \right) - s^k \right]^2 \right\} \quad (5)$$

where K denotes the number of GCPs. The essence of the single-image BA is to find a suitable parameter to minimize the target equation Q to solve for the affine transformation parameters $\boldsymbol{t}$ of the single-image. After $\boldsymbol{t}$ is calculated, the 3D geodetic coordinates of the GCPs are substituted into the RFM compensation model and combined with the regularization parameters to obtain the calculated image coordinates of the GCP, denoted (R_k^{cal}, C_k^{cal}), then the plane error of the kth GCPs is

$$\Delta \text{Error}_k = \sqrt{\left(R_k^{cal} - R_k^{true} \right)^2 + \left(C_k^{cal} - C_k^{true} \right)^2}. \quad (6)$$

The RMSE of plane error for single-image can be described as

$$\text{RMSE} = \sqrt{\sum_{k=1}^{K} \left(\left(R_k^{cal} - R_k^{true} \right)^2 + \left(C_k^{cal} - C_k^{true} \right)^2 \right) / K}. \quad (7)$$

To satisfy the consistency the GCPs that do not meet the conditions are eliminated and the BA is repeated until the convergence conditions are satisfied, which are as follows:

$$\begin{cases} \text{all} & \Delta \text{Error}_k \leq \text{TH} \cdot \text{RMSE} \\ or & K \leq 4 \end{cases} \quad (8)$$

where TH is the coefficient threshold. all is all point. In this study, TH is set to 5 for $\boldsymbol{L0}$ matching (i.e., coarse matching) and 2 for $\boldsymbol{Li}$ matching (i.e., fine matching).
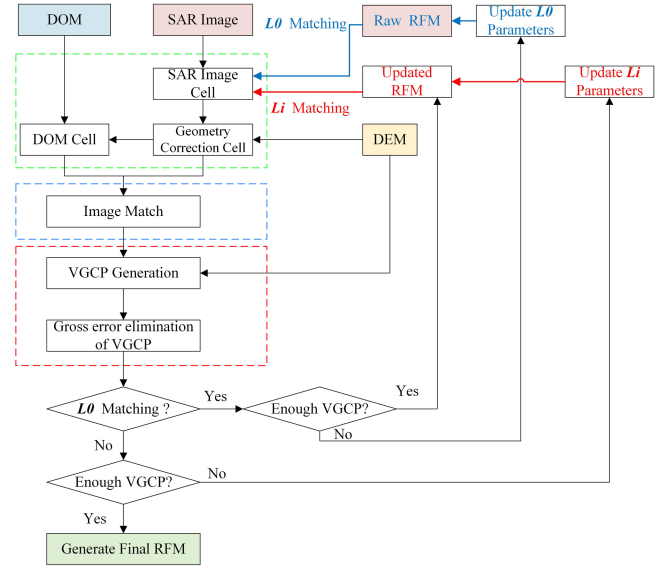

Fig. 3. Workflow of the proposed framework.

D. Multilevel and Multiscale SAR Image Matching

The multilevel multiscale times are related to the initial positioning error of satellite images. When the expected initial positioning error is large, the large-scale, low-resolution slices are first acquired for coarse matching and updating RFM. After reducing the initial positioning error, fine matching is carried out. At this time, to preserve the detailed features as much as possible, high-resolution slices can be acquired for matching. The workflow of the method is shown in Fig. 3.

1) Adaptive Matching Pair Acquisition: In $\boldsymbol{L0}$ matching (i.e., coarse matching), a large cell size is set and downsampled pairs of images are acquired at the same time [the resolution threshold is set to 3 (Tres = 3), the sampling resolution is the original SAR resolution multiplied by Tres]. Therefore, the spatial overlap of image pairs can be ensured, which solves the problem of matching failure due to the lack of overlap between image pairs caused by the initial positioning error. In $\boldsymbol{Li}$ matching (i.e., fine matching), because the initial RFM with LPEs has been initially corrected, small-sized cells but high-resolution image slices can be used to participate in the matching, to obtain a stable and sufficient number of matching points.

2) Image Match: In $\boldsymbol{L0}$ matching, it is recommended to use a feature-based method algorithm that is window-independent and insensitive to geometric offsets to obtain enough initial matching points, while a high-precision matching algorithm can be considered in the $\boldsymbol{Li}$ matching stage.

3) VGCPs Generation and Gross Error Elimination: The matching points of multiple image pairs are mapped into the whole SAR image coordinates and their corresponding 3D geodetic coordinates to form VGCPs, and the VGCPs with gross errors are eliminated.

4) RFM Update: Combined with VGCPs, the RFM model is updated using a method based on no terrain constraints, thus improving the original image positioning accuracy.
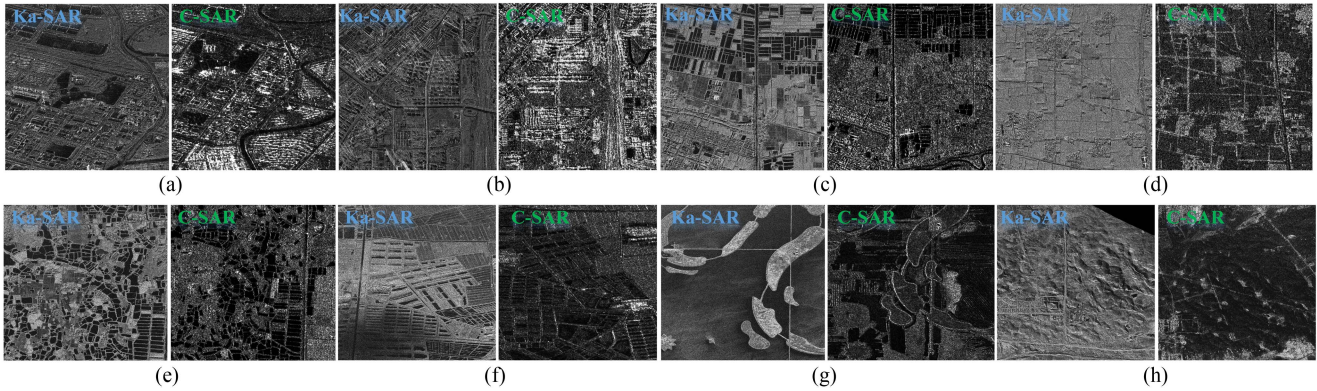
Fig. 4. Experimental images of different scenes. (a) City 1 (Simple). (b) City 2 (Difficult). (c) Suburb 1 (Simple). (d) Suburb 2 (Difficult). (e) Farmland 1 (Simple). (f) Farmland 1 (Difficult). (g) Water (Simple). (h) Hill (Difficult).

5) Multilevel and Multiscale Iterations: The iteration condition is based on whether it is an *L0* matching (i.e., coarse matching) and the number of matching points.

Step 1, *L0* matching: Because the initial positioning error of the image is unknown, to ensure that the *L0* matching can acquire a sufficient number of VGCPs and, thus, roughly correct the RFM, the matching results need to be judged.

If the number of VGCPs for initial matching is not enough, the *L0* parameters are updated and the cell size (Ker) is increased to ensure that there is enough overlap of image pairs.

If the number is satisfied, it is directly used for RFM updates.

Step 2, *Li* matching: If the number of VGCPs is insufficient, the *Li* parameters are updated to increase the cell size (Ker) while increasing the number of matching blocks.

If the number is enough, then update RFM directly and output it.

In this study, the number of VGCPs is set to 10, which can be modified according to the actual situation.

IV. EXPERIMENTS AND ANALYSIS OF MULTISOURCE SAR MATCHING

A. Analysis of Different Matching Algorithms for Ka/C SAR

1) Experimental Data: The wavelength ranges of C, X, and Ka are 37.5–75, 25–37.5, and 7.5–11.11 mm, respectively. Compared with the C/X band, the Ka band has a shorter wavelength, which is close to the visible light and can depict more details of ground objects. Most of the current matching algorithms for SAR images are based on homologous SAR images, such as C-band or X-band [23], and there are few reports on the matching studies for multisource SAR images. However, the huge difference between wavelengths inevitably brings challenges to multisource SAR images. In this study, the method utilizes the GF-3 DOM in the C-band to improve the positioning accuracy of LJ-2 images in the Ka-band. Therefore, the matching characteristics of Ka/C SAR are analyzed through experiments. Eight groups of Ka/C SAR image pairs are selected for the experiment, including five types of surface objects: city, suburb, farmland, water, and hill. Among them, two groups of image pairs were selected for city, town, and farmland, including simple and difficult levels.

The experimental image information is shown in Table I and Fig. 4.

Fig. 4 shows that Ka-SAR and C-SAR have great differences in radiation differences. The Ka-SAR image is derived from the LJ-2 image, with an original image resolution of 3 m and a local geometric correction resolution of 3.5 m. The C-SAR image comes from the GF-3 10 m DOM product, which is resampled to 3.5 m in this study.

2) Analysis: To explore the matching effect of different algorithms in Ka/C SAR images, experiments adopted SAR-SIFT [24], SIFT [25], HAPCG [26], HOWP [27], MOTIF [28], RIFT [29], CFOG [30], MS-HLMO [31], LNIFT [32], and POS-GIFT [33] totaling 10 SOTA algorithms are experiment on the test image pairs. In the experiment, the affine change model is adopted, and the error threshold is set to three pixels. SAR-SIFT is a specialized SAR matching algorithm, SIFT is an optical matching algorithm, and the rest of the algorithms are heterologous image matching algorithms. The number of correct matches (NCM) results are shown in Table II and Fig. 5.

In Table II, the top three NCM pairs of the same image were counted and marked in red. The results show that HAPCG, RIFT, and POS-GIFT perform well in Ka/C SAR images (red times are 6, 6, and 7, respectively). In addition, SAR-SIFT fails to match points in all three difficult scenes (City2, Suburb1, Hill), indicating that the matching between multisource SAR (Ka/C band in this study) is more difficult than that between homology SAR matching.

Although the matched points are processed by the mismatch point elimination method, the homonymous points obtained in difficult scenes even after this process are not completely correct. Therefore, the NCM in Table II cannot be used as a valid indicator, and manual interpretation is needed at this time. Fig. 6 shows the matching results of different scenes using 10 algorithms. Considering that the image pairs have been locally geometric corrected, the differences in scale and rotation are basically eliminated. In the matching process, the affine transformation model is used in the purification of matching points, and the matching result line should show the affine change law in theory. Therefore, the validity of the results is further determined by
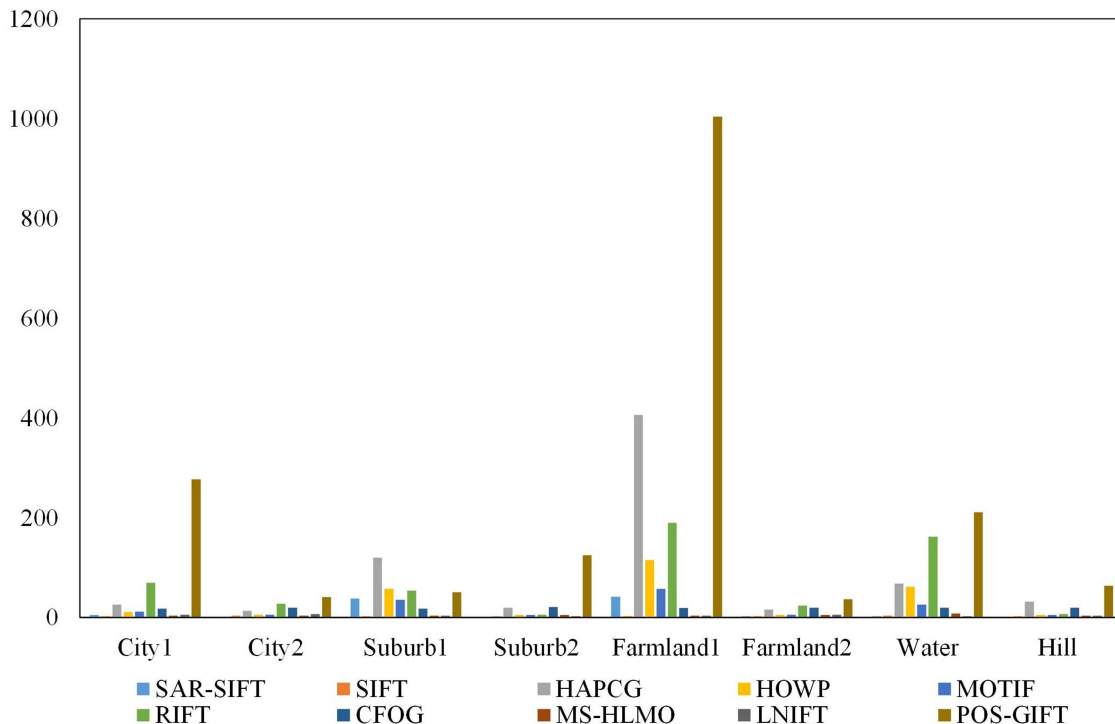
Fig. 5.   NCM results of different methods.

manual interpretation and labeled in Fig. 6, where the red √ marks indicate effective matching.

In Fig. 6, SAR-SIFT can match effectively for simple scenes such as City1, Suburb1, and Farmland1. However, the algorithm fails when the image radiation difference is large or the texture information is not rich. In Table II, although there are a few points in the statistical results of the SIFT algorithm, the manual interpretation in Fig. 6 reveals that they are all invalid matches. For simple scenes, most of the heterosource matching algorithms can perform effective matching, such as City1, Suburb1, Farmland1, and Water scenes. However, in difficult scenes, even with heteroscedastic matching algorithms, some of the methods are no longer applicable, reflecting the complexity of multisource SAR image matching.

Table III statistics the number of valid matches for different methods. The results show that both MOTIF and RIFT achieve effective matching in different scenes for seven times, followed by HOWP and POS-GIFT for five times and HAPCG for four times. SIFT is not suitable for SAR matching, and the number of effective matching is 0. The number of valid matches for CFOG is 0. The analysis shows that the CFOG algorithm needs good initial positioning results, and then template matching under the specified window can be carried out. In this experiment, the positioning error between the matched images is large (about 200 pixels), the CFOG algorithm fails. It should be noted that except for the affine transform parameter threshold modification (the threshold is 3 in this study), all other parameters are unchanged during the test in this study, which is the reason for the poor matching results of some algorithms such as MS-HLMO and

LNIFT. Considering the NCM and the number of effective matches, the RIFT method is selected for matching Ka/C SAR images. In practical applications, multiple matching methods can be used simultaneously to obtain stable matching points in the corresponding region.

B. Analysis of Positioning Errors on Image Matching

1) Experimental Data: To explore the effect of initial positioning error on matching, Optical/SAR and Ka/C SAR images were used for testing. For the Optical/SAR image pair, the initial offset (small offset) is in a few pixels, and a 100-pixel offset is added to the Optical image in the X and Y directions, respectively, and then it is composed with the original SAR image to form a large offset image pair (large offset). Ka/C SAR is an image pair composed of LJ-2 local geometric correction cell and GF-3 DOM cell, both with a resolution of 3.5 m. The small offset is in a few pixels and the error of the large offset is around 200 pixels, the image pairs are shown in Fig. 7.

2) Analysis: In Section IV-A, it is shown that CFOG, MS-HLMO, and LNIFT algorithms have poor matching results for Ka/C SAR images. To explore the effect of positioning error on the above three algorithms, small and large offset image pairs corresponding to Optical/SAR and Ka/C SAR are used for testing, and RIFT is used for comparison. Table IV shows the statistics of the NCM results, and Fig. 8 shows the matching results.

Table IV and Fig. 8 show that the number of NCM decreases in the presence of large offsets. Taking the RIFT algorithm as an
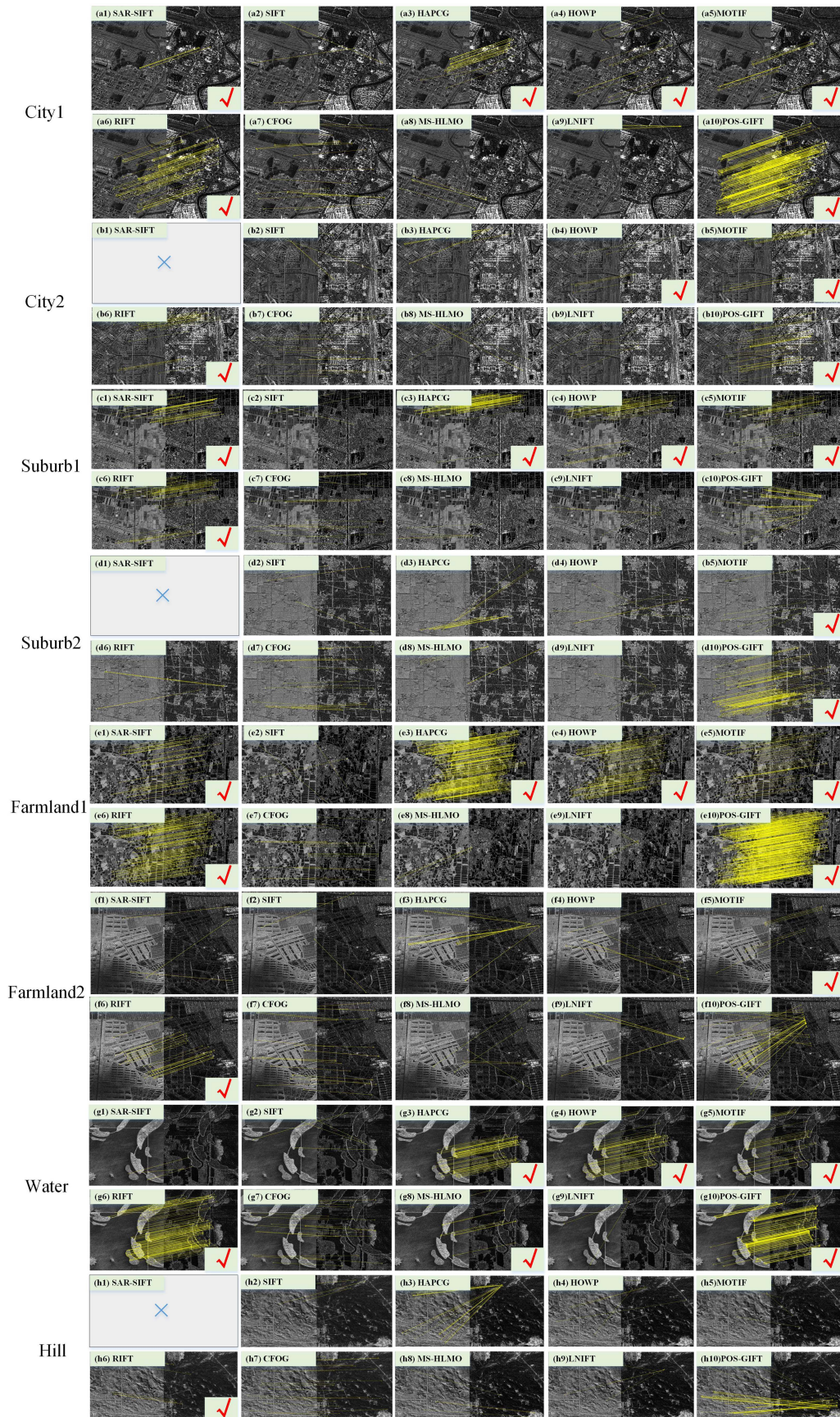
Fig. 6. Match results in different scenes and methods.

Algorithm 1: VGCPMF Algorithm.

Input: SAR Image, Raw RFM, DOM, and DEM data;
Output: VGCPs and Final RFM;
Parameter: FLAG = *L0* matching, *M0* = 2, *Mi* = 1;
1:   **do**
     // 1) Adaptive matching pair acquisition
2:     **if** *L0* matching = = FLAG
      // @ *L0* matching parameters
3:       Set: *nGX* = 2, *nGY* = 15, *TH* = 5, *Tres* = 3;
4:       *Ker* = *M0* ∗ 1024;
5:       RFM = raw RFM;
6:     **end if**
7:     **if** *Li* matching = = FLAG
      // @ *Li* matching parameter
8:       Set: *nGX* = 3, *nGY* = 30, *TH* = 2, *Tres* = 2;
9:       *Ker* = *Mi* ∗ 1024;
10:      RFM = updated RFM;
11:     **end if**
12:     **for** (i = 1; $i \le nGX$; i ++)
13:       **for** (j = 1; $j \le nGY$; j ++)
14:         Image cell construction accroding to (2) and (1);
15:         DOM cell and geometry correction cell generation;
16:         Image match; // 2) Image match
17:       **end for**
18:     **end for**
     // 3) VGCPs generation and gross error elimination
19:     VGCPs Generation;
20:     Gross error elimination accroding to (8);
21:     **if** nVGCPs < 10 // number of VGCPs denotes nVGCPs
22:       **if** *L0* matching = = FLAG
23:         *M0* = *M0* + 1;
24:       **end if**
25:       **if** *Li* matching = = FLAG
26:         *Mi* = *Mi* + 1;
27:       **end if**
28:       **else**
29:         **if** *L0* matching = = FLAG
30:           FLAG = *Li* matching;
31:           RFM update; // 4) RFM update
32:         **end if**
33:       **end if**
34:     **while** (nVGCPs $\ge$ 10 and *Li* matching = = FLAG)
35:     Generate Final RFM; // 4) RFM update
36:     return VGCPs and Final RFM;

---

example, the NCM of Optical/SAR, Ka/C SAR, and small and large offsets are 451/326 and 621/270, respectively. The effect of offset on the number of matching points is more significant in the Ka/C SAR image pair. For the Optical/SAR pair, the result shows that the NCM of MS-HLMO and LNIFT are 28/10 and 224/111 for small and large offsets, respectively, and the reduction of the number of points of the NCM is more than half. For CFOG, it is manually interpreted as an invalid match at a large offset.

TABLE I
EXPERIMENTAL IMAGES INFORMATION

| Test Image	level	Size(Pixel)	Image characteristic
City1	Simple	629×876	Structural information is obvious
City2	Difficult	864×910	Built area, heavy layover
Suburb1	Simple	872×924	Rich textures
Suburb2	Difficult	760×828	Significant radiation differences
Farmland1	Simple	869×918	Rich textures
Farmland2	Difficult	626×876	Significant radiation differences
Water	Simple	753×826	Significant radiation differences
Hill	Difficult	885×846	Significant radiation differences, weak texture
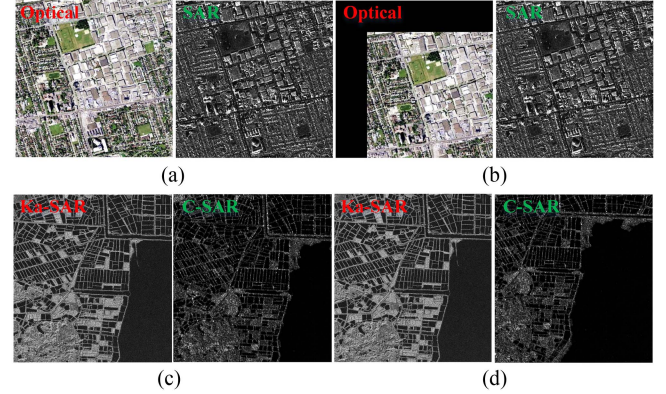
Fig. 7. Small and large offset image pairs. (a) Small offset. (b) Large offset. (c) Small offset. (d) Large offset.

Fig. 8(c3), (d3), (c4), and (d4) are manually interpreted as invalid matches, and the results show that MS-HLMO and LNIFT cannot be adapted to Ka/C SAR matching.

Further analysis shows that the Ka/C SAR image pair has a large difference in resolution. The GF-3 DOM (C-SAR) has an original resolution of 10 m. Although it is sampled to 3.5 m, the effective information does not increase. In addition, the speckle noise of the image pair is not suppressed, which may cause the failure of the matching algorithm. CFOG can achieve good results in small offsets of Ka/C SAR, but the algorithm fails when there are large offsets.

Experiments show that large offsets inevitably lead to a decrease in the NCMs. For Ka/C SAR image matching, the offset between the images, i.e., the positioning error of the images, needs to be considered. When a large offset (positioning error) exists, a robust feature-based matching algorithm is used as much as possible. After initially eliminating the large offset (positioning error), template matching or other matching algorithms with higher accuracy can be used to obtain more matching points. In addition, Ka/C SAR images are more difficult to match than Optical/SAR or homologous SAR images due to the difference in speckle noise and backscattering characteristics of different bands in SAR images. The algorithm can be improved according to the image characteristics between Ka/C SAR.

V. LJ-2 IMAGE ACCURACY IMPROVEMENT AND VERIFICATION

The LJ-2 satellite has been in orbit for more than one year since it was successfully launched in Jiuquan, China, on May 21,

TABLE II
STATISTICS OF NCM RESULT IN DIFFERENT SCENES

Method	City1 Simple	City2 Difficult	Suburb1 Simple	Suburb2 Difficult	Farmland1 Simple	Farmland2 Difficult	Water Simple	Hill Difficult
SAR-SIFT	5	0	38	0	42	3	3	0
SIFT	3	4	3	3	3	3	4	3
HAPCG	26	14	120	20	406	16	68	32
HOWP	11	6	58	5	115	5	62	5
MOTIF	12	6	36	5	58	6	26	5
RIFT	70	28	54	6	190	24	162	7
CFOG	18	20	18	21	19	20	20	20
MS-HLMO	4	4	4	5	4	5	8	4
LNIFT	6	7	4	3	4	6	3	4
POS-GIFT	277	41	51	125	1004	37	211	64

The top three NCM pairs of the same image were counted and marked in red.

TABLE III
NUMBER OF VALID MATCHES FOR DIFFERENT METHODS

Method	SAR-SIFT	SIFT	HAPCG	HOWP	MOTIF	RIFT	CFOG	MS-HLMO	LNIFT	POS-GIFT
Times	3	0	4	5	7	7	0	1	0	5
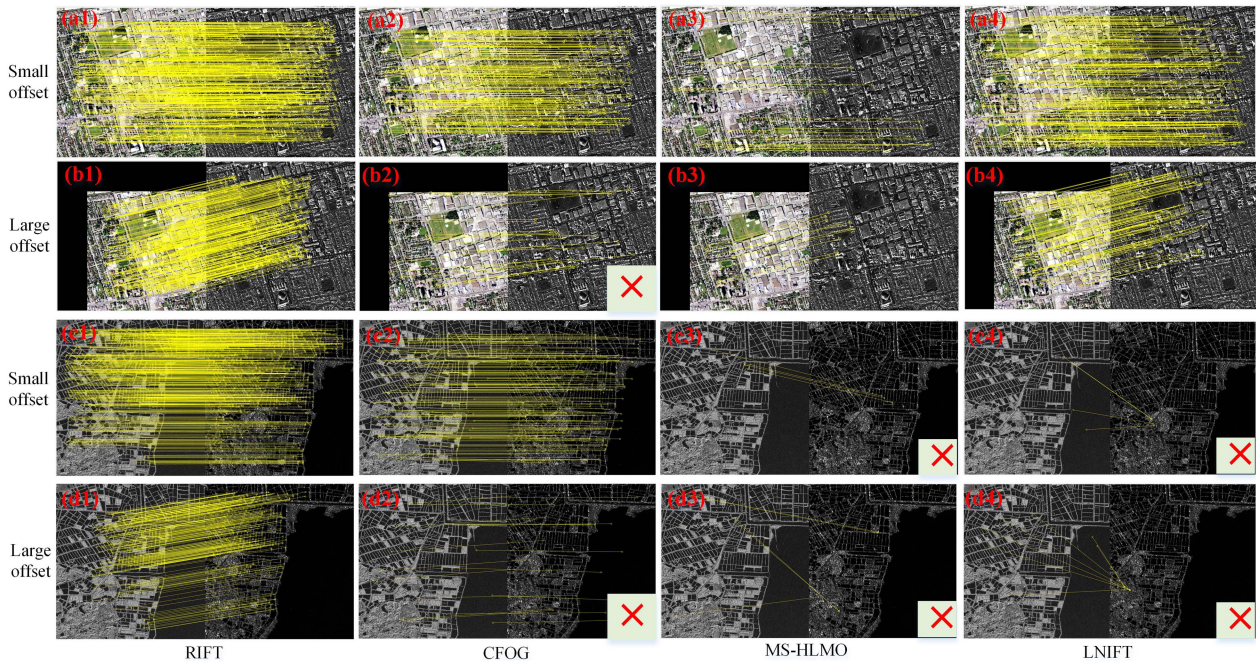
Fig. 8. Match results of small and large offset image pairs: the red × marks an invalid match.

TABLE IV
NCM RESULTS FOR DIFFERENT INITIAL ERROR IMAGE PAIRS

Category	Offset	RIFT	CFOG	MS-HLMO	LNIFT
Optical/SAR	Small offset	451	200	28	224
	large offset	326	24	10	111
Ka/C-SAR	Small offset	621	179	4	4
	large offset	270	18	5	7

2023. The satellite is commonly used for stripmap mode image products. The accuracy of the product has not been publicly

reported so far. The experiment adopts LJ-2 stripmap mode images combined with the proposed method to process these images and verify the accuracy.

A. Experimental Data

In this study, the 3-m resolution stripmap mode image of LJ-2 was used for experiments. The image information of five images is shown in Fig. 9 and Table V. The DOM data were obtained from GF-3 DOM with 10-m resolution and better than 10-m accuracy [34], [35], and the elevation data were obtained from AW3D products.
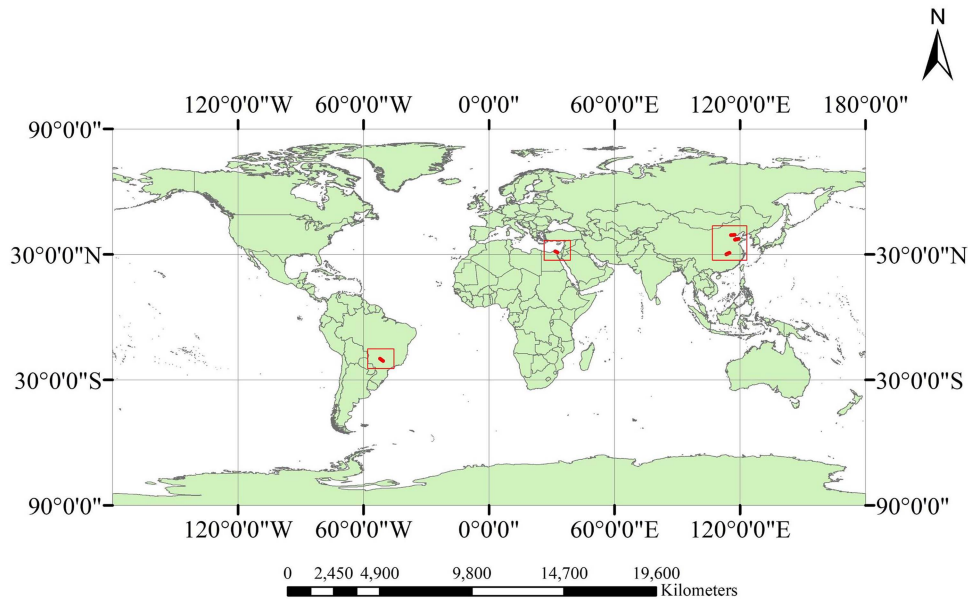
Fig. 9.   LJ-2 image distribution.

TABLE V
LJ-2 IMAGES INFORMATION FOR DIFFERENT AREAS

Area	Time	Orbit	Size (Pixel)	Center
Tianjin(China)	2023.07.31	ASC	4065×211250	39.3379°N, 116.5865°E
Dongying(China)	2023.07.24	ASC	4237×187500	37.2733°N, 118.4765°E
Wuhan(China)	2023.07.18	ASC	4661×237150	30.4455°N, 114.197°E
Egypt	2023.12.05	DESC	3440×111400	31.2345°N, 32.2427°E
Brazil	2023.10.30	DESC	4858×226400	20.3799°S, 51.3707°W

B. Feasibility Analysis of the Proposed Method

To verify the feasibility of the proposed method, the image of Wuhan is selected for experiments. Due to the LPE of the LJ-2 image, to ensure that the geometric correction cell overlaps with the corresponding DOM cell, the larger cell size is set for *L0* matching (*Ker* = 2048). Meanwhile, to increase the matching speed, the resolution threshold is set to 3 (Tres = 3) (The sampling resolution is the original SAR resolution multiplied by Tres) to achieve a balance between taking into account the geographic range and size of the image. Considering that the LJ-2 stripmap mode image is long (Wuhan image size 4661×237150), at this time, *nGX* and *nGY* are set to 2 and 15, respectively. The results of *L0* matching are mainly used to roughly correct the original RFM, so the threshold TH [in (8)] is set to 5 in the gross error elimination. In *Li* matching, the grid division is more uniform, *nGX* and *nGY* are set to 3 and 30, respectively, while *Ker* = 1024 and Tres = 2 are set. After the RFM is updated with *L0* matching results, the positioning error of the image is reduced at this time, and the smaller cell size and higher sampling multiplier can be used to obtain the local fine feature information, and better matching results can be obtained.

Fig. 10 shows the distribution of VGCPs in different stages. It can be seen in Fig. 10(a) and (c) that the grid division strategy

of this study combined with the RIFT matching algorithm can obtain uniformly distributed VGCPs, both in the *L0* matching stage and the *Li* matching stage. The method still retains the effective VGCPs even after gross error elimination, see Fig. 10(b) and (d). The experiments show that the multilevel multiscale matching method in this study is effective.

To further show the effect, the original RFM and the updated RFM of the proposed method are used to indirectly correct the image and superimposed with the GF-3 DOM respectively, and the results are shown in Fig. 11.

Fig. 11 shows that the LJ-2 image has a large offset from the DOM. After processing by the proposed method, there is no offset with DOM and it can fit perfectly. The experimental results verify that the method of this study can realize the high-precision geometric processing of the micro SAR (LJ-2) image under the LPE.

C. Improvement of Image Positioning Accuracy in Different Areas

In this experiment, the same method is used to obtain the VGCPs of multiscenes images. Some of these VGCPs are used as independent check points (ICPs) to evaluate the positioning accuracy of LJ-2 images. Two schemes of 0 GCPs and 4 GCPs were used in the experiment to evaluate the GPA of
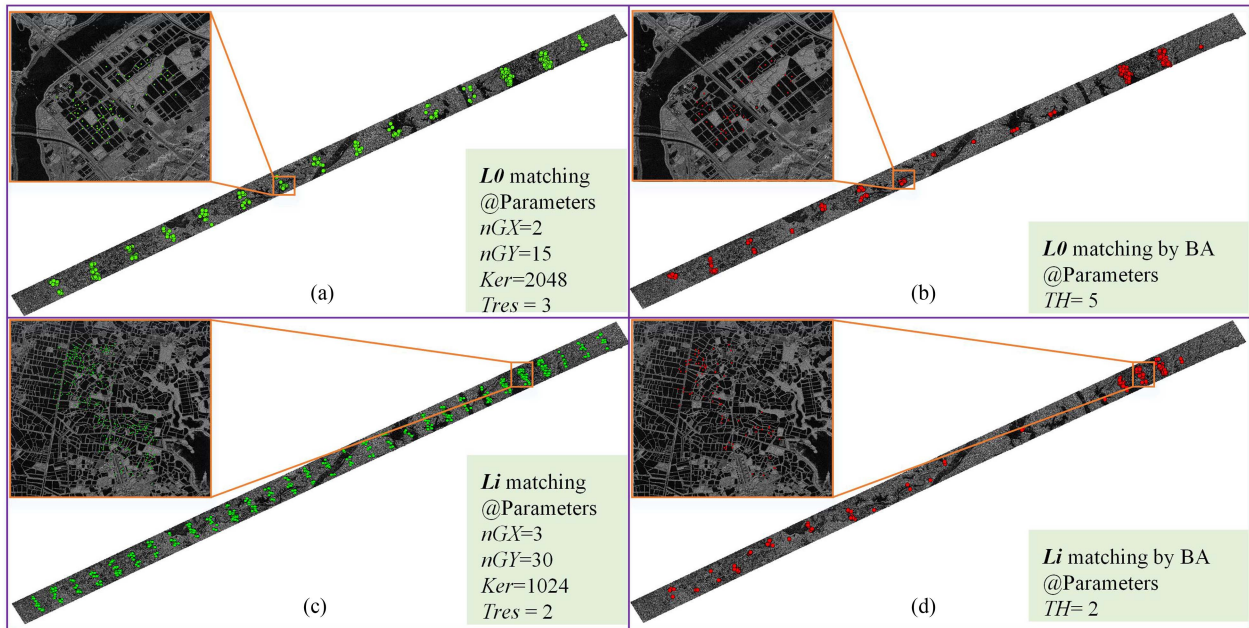
Fig. 10. Distribution of VGCPs in different stages. (a) *L0* matching. (b) *L0* matching by BA. (c) *Li* matching. (d) *Li* matching by BA.
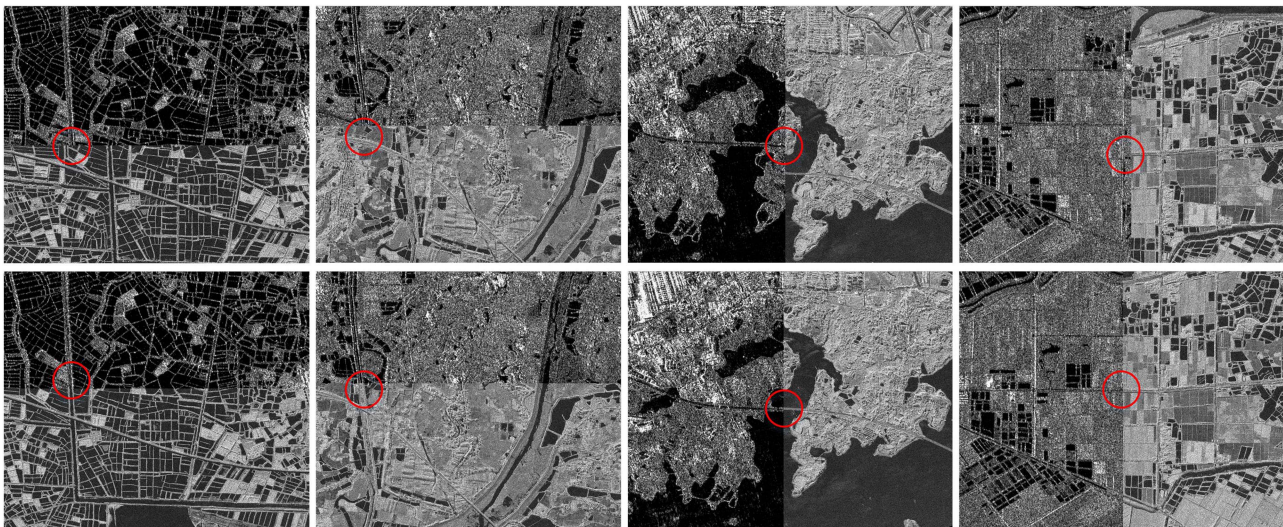

Fig. 11. Comparison between the original positioning results and the processed results by the proposed method: the first line is the original results, and the second line is the processed results.

LJ-2 images in different areas, and the results are shown in Table VI and Figs. 12–16. In this experiment, it no longer distinguishes between VGCPs and GCPs but uses GCPs for a unified representation. Wuhan image control points are directly used to participate in the accuracy assessment because they have been generated in Section V-B.

In Table VI and Figs. 12–16, the BA results of the 0 GCP scheme show that the residual distributions of the ICPs are consistent in magnitude and direction, and it can be assumed that the error distributions satisfy the assumption of affine transformation in the image space. After compensating for the systematic error, the residual distribution of the checkpoints shows

randomness, indicating that the systematic error is effectively eliminated.

The results in Table VI show that the initial planar positioning accuracy of the five scene images in the global range is between 650 and 950 m. After high-precision processing, the planar accuracy can reach better than 5 m, and the GPA is improved significantly, which reflects the effectiveness of the proposed method.

Further analysis shows that the error in the east direction of Tianjin, Dongying, and Brazil is smaller than that in the north direction, while the error in the east direction of Wuhan and Egypt is larger than that in the north direction, which shows

TABLE VI
GEOMETRIC POSITIONING RESULTS FOR DIFFERENT AREAS

Area	GCPs	ICPs	Max error of ICPs(m)			RMSE of ICPs(m)		
			E	N	planar	E	N	planar
Tianjin	0	30	402.269	690.607	799.224	390.697	675.483	780.334
(China)	4	26	2.213	8.353	8.475	1.137	3.560	3.737
Dongying	0	118	443.369	585.743	733.655	438.436	576.006	723.884
(China)	4	114	3.268	7.021	7.026	1.287	2.722	3.011
Wuhan	0	304	517.776	448.002	669.531	492.824	434.234	656.836
(China)	4	300	3.640	6.275	6.275	1.584	2.643	3.081
Egypt	0	88	674.747	587.130	891.669	658.914	574.696	874.325
	4	84	5.654	6.816	8.221	2.076	2.886	3.555
Brazil	0	21	538.041	817.257	962.681	500.640	801.502	945.011
	4	17	4.784	6.584	7.491	2.660	3.329	4.261
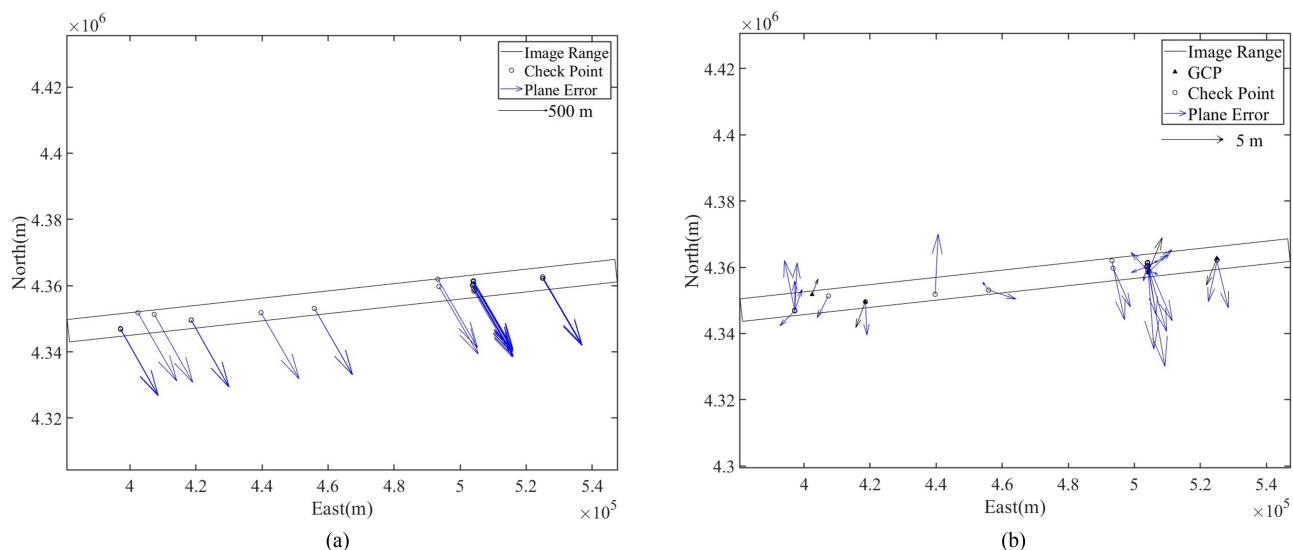
Fig. 12.   Residual errors of bundle adjustment for Tianjin area. (a) 0 GCP. (b) 4 GCP.
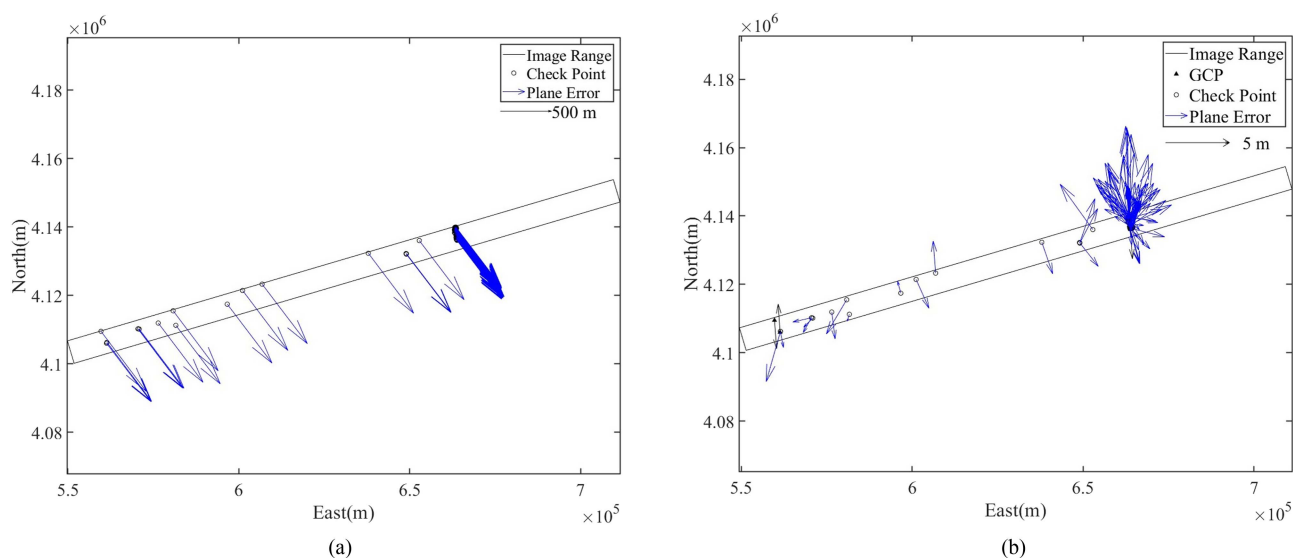
Fig. 13.   Residual errors of bundle adjustment for Dongying area. (a) 0 GCP. (b) 4 GCP.
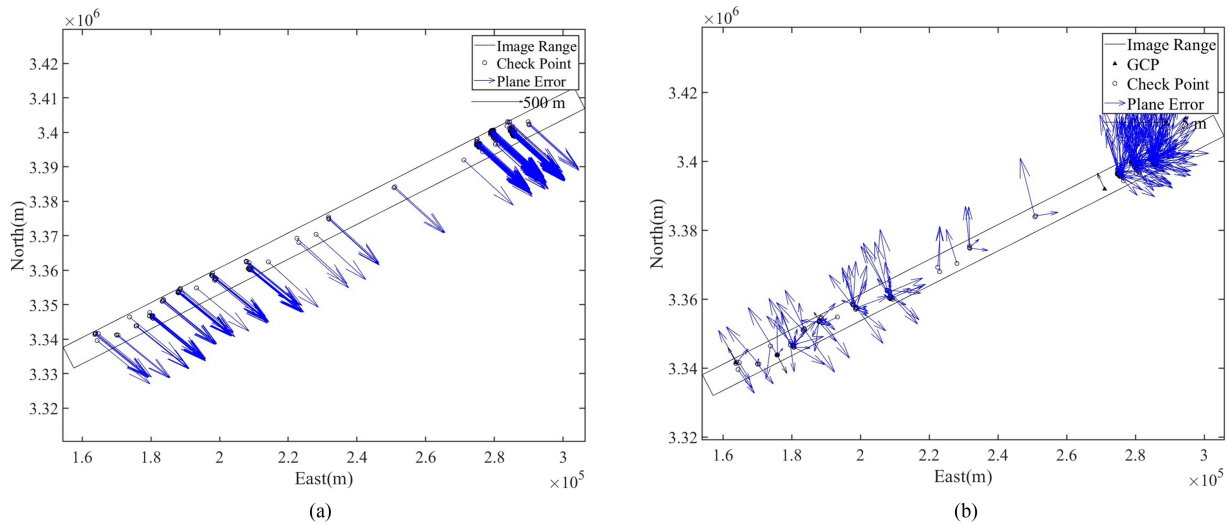
Fig. 14. Residual errors of bundle adjustment for Wuhan area. (a) 0 GCP. (b) 4 GCP.
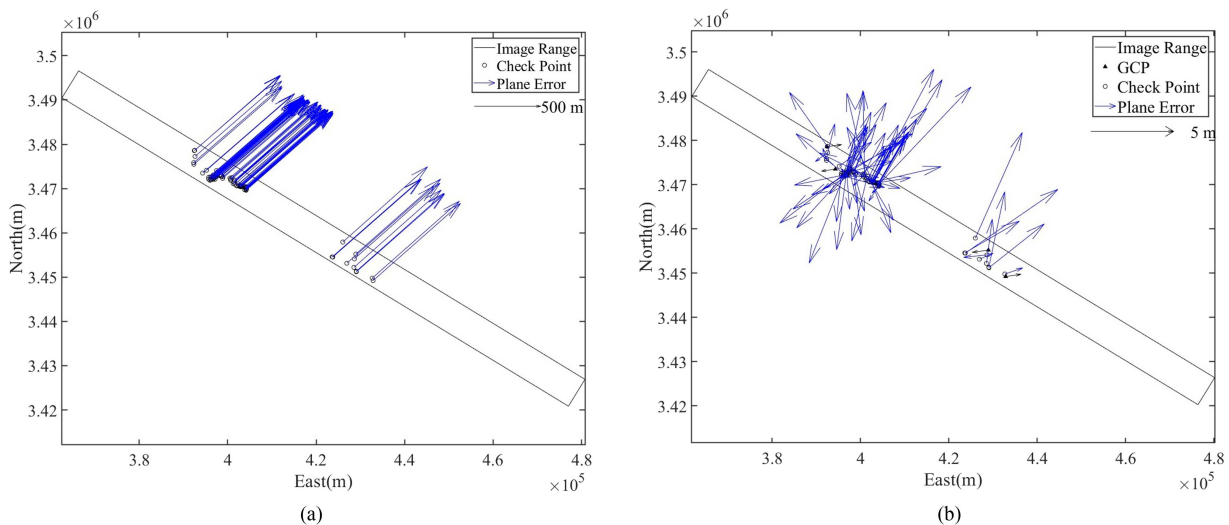
Fig. 15. Residual errors of bundle adjustment for Egypt area. (a) 0 GCP. (b) 4 GCP.

inconsistency. The subsequent study can decompose the errors based on the high-precision calibration field data, and then compensate the errors to obtain higher positioning accuracy.

Fig. 17 shows the orthophoto products of LJ-2 superimposed with GF-3 DOM after high-precision geometric processing. Owing to the results of the Wuhan area have been explained in Section V-B, only the results of Tianjin, Dongying, Egypt, and Brazil are shown here. The results show that the orthophoto products generated by the proposed method have no misalignment with GF-3 DOM in both domestic and foreign regions, which verifies the validity of this method, and can provide support for the high-precision geometric processing of LJ-2 data on a global scale.

VI. DISCUSSION

In this study, multiple sets of data are used to perform matching experiments on SAR images under large offsets. In

Table IV, the NCM of different matching algorithms in the presence of small and large offsets are counted. For the RIFT algorithm, the NCM of Optical/SAR, Ka/C SAR, and small and large offsets are 451/326 and 621/270, respectively. The offset results in a reduction of 27.7% and 56.5% in the two image pairs, respectively. For the CFOG algorithm, the NCM of Optical/SAR, Ka/C SAR, and small and large offsets are 200/24 and 179/18, respectively. The offset results in a reduction of 88.0% and 89.9% in the two image pairs, respectively. The results show that geometric offset can significantly reduce image-matching performance. Different matching algorithms have different sensitivity to the geometric offset. In addition, it can be found that the number of matched points on the Ka/C SAR image pair is less than on the Optical/SAR image pair, indicating the complexity of matching between Ka/C SAR images.

Further analysis shows that for the Optical/SAR image pair, speckle noise only appears on the SAR image. However, due
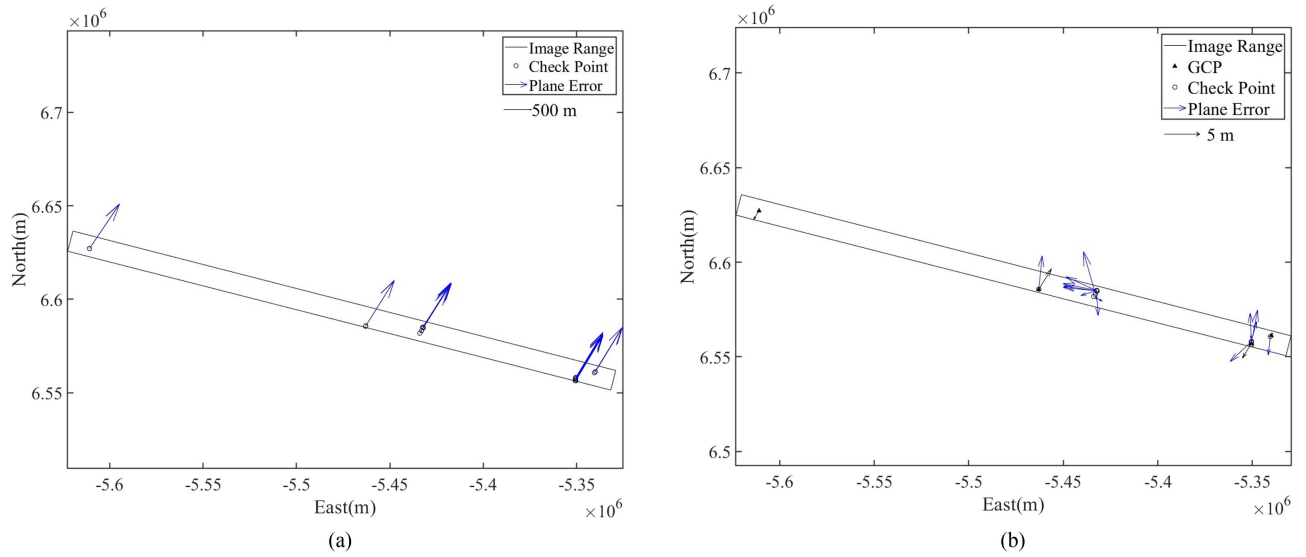
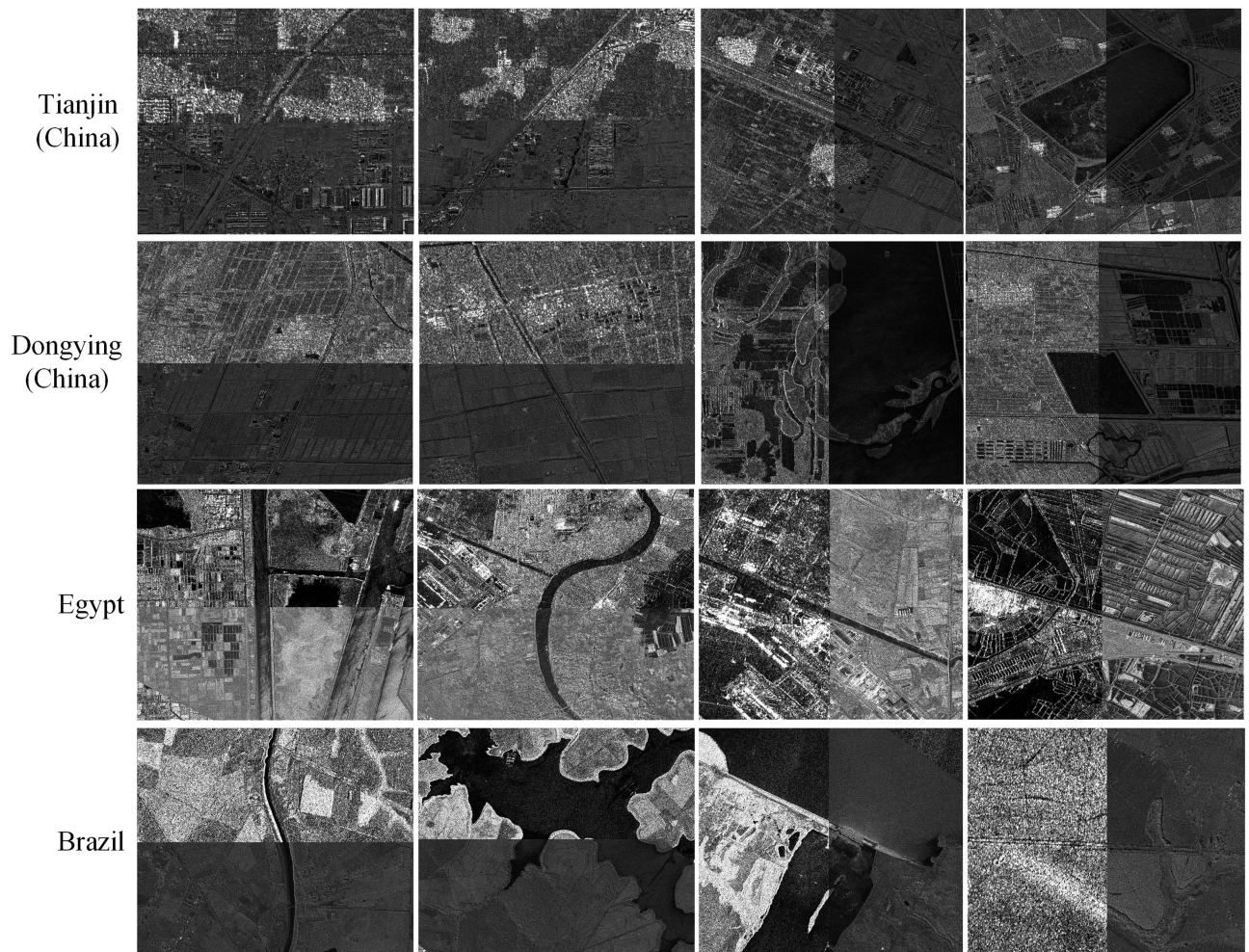Fig. 16. Residual errors of bundle adjustment for Brazil area. (a) 0 GCP. (b) 4 GCP.

Fig. 17. Results of high-precision geometric processing in different areas.

to the difference in wavelength of Ka/C image pairs (C-band: 37.5–75 mm, Ka-band: 7.5–11.11 mm), the distribution of speckle noise on Ka-SAR and C-SAR images is different. The coupling of many complex conditions makes it difficult to match the Ka/C SAR image pair.

There is currently no matching algorithm specifically for Ka/C SAR images. The algorithm needs to be improved subsequently for the Ka/C SAR image characteristics. In this study, based on the comparison and analysis of several sets of experiments, we found that RIFT can achieve better results. Therefore, the RIFT algorithm is recommended as the preferred algorithm for matching between Ka/C SAR images.

Although the proposed method can automatically extract VGCPs under small and large offsets, there are limitations. First, it requires initial range prediction with the help of RFM, which no longer applies in the absence of RFM. Second, the multiple local geometric corrections in multilevel iterations require more memory requirements and will be less efficient.

VII. Conclusion

Microsatellites (e.g., micro-optical or SAR satellites) have the problem of large initial positioning errors. However, compared with other microsatellites, it is more difficult to match micro SAR satellite images with other control data. The proposed method first designs a multilevel and multiscale SAR image-matching framework. Then it selects the RIFT algorithm as the multisource SAR matching algorithm based on 10 SOTA algorithms and finally realizes the high-precision VGCPs extraction between the micro SAR satellite image and the SAR DOM under the case of LPE. Therefore, the micro SAR satellite image positioning accuracy can be improved based on the VGCPs. Experiments were conducted using five SAR images (LJ-2 stripmap mode). Meanwhile, the GF-3 DOM was used as control data. The results show that the GPA of the LJ-2 image is at the kilometer level, and it can be improved to better than 5 m (relative to GF-3 DOM) after processing, which proves the validity and reliability of the proposed method. The proposed method can provide support for the cooperative processing of multisource SAR satellite image data. The high-precision LJ-2 products processed by the proposed method can, therefore, be used in such fields as marine environment monitoring and protection, disaster monitoring and evaluation of water conservancy facilities, and meteorology.

Acknowledgment

References

[1] V. Ignatenko, P. Laurila, A. Radius, L. Lamentowski, O. Antropov, and D. Muff, "ICEYE microsatellite SAR constellation status update: Evaluation of first commercial imaging modes," in *Proc. IEEE Int. Geosci. Remote Sens. Symp.*, Sep. 2020, pp. 3581–3584, doi: 10.1109/IGARSS39084.2020.9324531.

[2] C. Stringham et al., "The capella X-band SAR constellation for rapid imaging," in *Proc. IEEE Int. Geosci. Remote Sens. Symp.*, Jul. 2019, pp. 9248–9251, doi: 10.1109/IGARSS.2019.8900410.

[3] N. Jiao, F. Wang, H. You, J. Liu, and X. Qiu, "A generic framework for improving the geopositioning accuracy of multi-source optical and SAR imagery," *ISPRS J. Photogramm. Remote Sens.*, vol. 169, pp. 377–388, Nov. 2020, doi: 10.1016/j.isprsjprs.2020.09.017.

[4] T. Long, W. Jiao, G. He, R. Yin, G. Wang, and Z. Zhang, "Block adjustment with relaxed constraints from reference images of coarse resolution," *IEEE Trans. Geosci. Remote Sens.*, vol. 58, no. 11, pp. 7815–7828, Nov. 2020, doi: 10.1109/TGRS.2020.2984533.

[5] G. Zhang, B. Jiang, T. Wang, Y. Ye, and X. Li, "Combined block adjustment for optical satellite stereo imagery assisted by spaceborne SAR and laser altimetry data," *Remote Sens.*, vol. 13, no. 16, Aug. 2021, Art. no. 3062, doi: 10.3390/rs13163062.

[6] H. Bagheri, M. Schmitt, P. d'Angelo, and X. X. Zhu, "A framework for SAR-optical stereogrammetry over urban areas," *ISPRS J. Photogramm. Remote Sens.*, vol. 146, pp. 389–408, Dec. 2018, doi: 10.1016/j.isprsjprs.2018.10.003.

[7] N. Jiao, F. Wang, and H. You, "A new combined adjustment model for geolocation accuracy improvement of multiple sources optical and SAR imagery," *Remote Sens.*, vol. 13, no. 3, Jan. 2021, Art. no. 491, doi: 10.3390/rs13030491.

[8] R. Zhao, G. Zhang, M. Deng, K. Xu, and F. Guo, "Geometric calibration and accuracy verification of the GF-3 satellite," *Sensors*, vol. 17, no. 9, Aug. 2017, Art. no. 1977, doi: 10.3390/s17091977.

[9] G. Zhang, B. Jiang, T. Wang, Y. Ye, and X. Li, "Combined block adjustment for optical satellite stereo imagery assisted by spaceborne SAR and laser altimetry data," *Remote Sens.*, vol. 13, no. 16, Aug. 2021, doi: 10.3390/rs13163062.

[10] H. Pan, Z. Zou, G. Zhang, X. Zhu, and X. Tang, "A penalized spline-based attitude model for high-resolution satellite imagery," *IEEE Trans. Geosci. Remote Sens.*, vol. 54, no. 3, pp. 1849–1859, Mar. 2016, doi: 10.1109/TGRS.2015.2489382.

[11] A. F. Habib, M. Morgan, and Y. Lee, "Bundle adjustment with self–Calibration using straight lines," *Photogramm. Rec.*, vol. 17, no. 100, pp. 635–650, Oct. 2002, doi: 10.1111/0031-868X.00211.

[12] H. Zhang, G. Zhang, Y. Jiang, and T. Wang, "A SRTM-DEM-controlled ortho-rectification method for optical satellite remote sensing stereo images," *Acta Geod. Cartogr. Sin.*, vol. 45, no. 3, pp. 326–331+378, 2016, doi: 10.11947/j.AGCS.2016.20150358.

[13] Th. Toutin, C. V. Schmitt, and H. Wang, "Impact of no GCP on elevation extraction from WorldView stereo data," *ISPRS J. Photogramm. Remote Sens.*, vol. 72, pp. 73–79, Aug. 2012, doi: 10.1016/j.isprsjprs.2012.05.009.

[14] Y. Zhang, M. Zheng, X. Xiong, and J. Xiong, "Multistrip bundle block adjustment of ZY-3 satellite imagery by rigorous sensor model without ground control point," *IEEE Geosci. Remote Sens. Lett.*, vol. 12, no. 4, pp. 865–869, Apr. 2015, doi: 10.1109/LGRS.2014.2365210.

[15] S. Tang, B. Wu, and Q. Zhu, "Combined adjustment of multi-resolution satellite imagery for improved geo-positioning accuracy," *ISPRS J. Photogramm. Remote Sens.*, vol. 114, pp. 125–136, Apr. 2016, doi: 10.1016/j.isprsjprs.2016.02.003.

[16] G. Zhang, Y. Jiang, L. Li, M. Deng, and R. Zhao, "Research progress of high-resolution optical/SAR satellite geometric radiometric calibration," *Acta Geod. Cartogr. Sin.*, vol. 48, no. 12, pp. 1604–1623, 2019, doi: 10.11947/j.AGCS.2019.20190469.

[17] D. O. Nitti et al., "Automatic GCP extraction with high resolution COSMO-SkyMed products," *Proc. SPIE*, vol. 10003, Oct. 2016, Art. no. 1000302, doi: 10.1117/12.2241281.

[18] R. Werninghaus and S. Buckreuss, "The TerraSAR-X mission and system design," *IEEE Trans. Geosci. Remote Sens.*, vol. 48, no. 2, pp. 606–614, Feb. 2010, doi: 10.1109/TGRS.2009.2031062.

[19] R. Zhao, G. Zhang, M. Deng, F. Yang, Z. Chen, and Y. Zheng, "Multimode hybrid geometric calibration of spaceborne SAR considering atmospheric propagation delay," *Remote Sens.*, vol. 9, no. 5, May 2017, Art. no. 464, doi: 10.3390/rs9050464.

[20] M. Deng, G. Zhang, R. Zhao, S. Li, and J. Li, "Application of the atmospheric delay correction model in YG-13A range calibration," *J. Remote Sens.*, vol. 22, no. 3, pp. 373–380, 2018, doi: 10.11834/jrs.20187116.

[21] Q. Cheng et al., "MSRSI-TPMF: A tie points matching framework of Multisource remote sensing images," *IEEE J. Sel. Top. Appl. Earth Obs. Remote Sens.*, vol. 17, pp. 1623–1637, 2024, doi: 10.1109/JSTARS.2023.3331251.

[22] H. Wang et al., "Layover compensation method for regional spaceborne SAR imagery without GCPs," *IEEE Trans. Geosci. Remote Sens.*, vol. 59, no. 10, pp. 8367–8381, Oct. 2021, doi: 10.1109/TGRS.2020.3045505.

[23] X. Li et al., "SARPointNet: An automated feature learning framework for spaceborne SAR image registration," *IEEE J. Sel. Top. Appl. Earth Obs. Remote Sens.*, vol. 15, pp. 6371–6381, Aug. 2022, doi: 10.1109/JSTARS.2022.3196383.

[24] F. Dellinger, J. Delon, Y. Gousseau, J. Michel, and F. Tupin, "SAR-SIFT: A SIFT-like algorithm for SAR images," *IEEE Trans. Geosci. Remote Sens.*, vol. 53, no. 1, pp. 453–466, Jan. 2015, doi: 10.1109/TGRS.2014.2323552.

[25] D. G. Lowe, "Distinctive image features from scale-invariant keypoints," *Int. J. Comput. Vis.*, vol. 60, no. 2, pp. 91–110, Nov. 2004, doi: 10.1023/B:VISI.0000029664.99615.94.

[26] Y. Yao, Y. Zhang, Y. Wan, X. Liu, and H. Guo, "Heterologous images matching considering anisotropic weighted moment and absolute phase orientation," *Geomat. Inf. Sci. Wuhan Univ.*, vol. 46, no. 11, pp. 1727–1736, 2021, doi: 10.13203/j.whugis20200702.

[27] Y. Zhang et al., "Histogram of the orientation of the weighted phase descriptor for multi-modal remote sensing image matching," *ISPRS J. Photogramm. Remote Sens.*, vol. 196, pp. 1–15, Feb. 2023, doi: 10.1016/j.isprsjprs.2022.12.018.

[28] Y. Yao, B. Zhang, Y. Wan, and Y. Zhang, "Motif: Multi-orientation tensor index feature descriptor for sar-optical image registration," *Int. Arch. Photogramm. Remote Sens. Spat. Inf. Sci.*, vol. XLIII-B2-2022, pp. 99–105, May 2022, doi: 10.5194/isprs-archives-XLIII-B2-2022-99-2022.

[29] J. Li, Q. Hu, and M. Ai, "RIFT: Multi-modal image matching based on radiation-variation insensitive feature transform," *IEEE Trans. Image Process.*, vol. 29, pp. 3296–3310, Dec. 2019020, doi: 10.1109/TIP.2019.2959244.

[30] Y. Ye, L. Bruzzone, J. Shan, F. Bovolo, and Q. Zhu, "Fast and robust matching for multimodal remote sensing image registration," *IEEE Trans. Geosci. Remote Sens.*, vol. 57, no. 11, pp. 9059–9070, Nov. 2019, doi: 10.1109/TGRS.2019.2924684.

[31] C. Gao, W. Li, R. Tao, and Q. Du, "MS-HLMO: Multiscale histogram of local main orientation for remote sensing image registration," *IEEE Trans. Geosci. Remote Sens.*, vol. 60, Jul. 2022, Art. no. 5626714, doi: 10.1109/TGRS.2022.3193109.

[32] J. Li, W. Xu, P. Shi, Y. Zhang, and Q. Hu, "LNIFT: Locally normalized image for rotation invariant multimodal feature matching," *IEEE Trans. Geosci. Remote Sens.*, vol. 60, Apr. 2022, Art. no. 5621314, doi: 10.1109/TGRS.2022.3165940.

[33] Z. Hou, Y. Liu, and L. Zhang, "POS-GIFT: A geometric and intensity-invariant feature transformation for multimodal images," *Inf. Fusion*, vol. 102, Feb. 2024, Art. no. 102027, doi: 10.1016/j.inffus.2023.102027.

[34] T. Wang et al., "Large-scale orthorectification of GF-3 SAR images without ground control points for China's land area," *IEEE Trans. Geosci. Remote Sens.*, vol. 60, Jan. 2022, Art. no. 5221617, doi: 10.1109/TGRS.2022.3142372.

[35] X. Li, B. Jiang, T. Wang, G. Zhang, H. Cui, and Q. Cheng, "Geometric positioning accuracy improvement method without ground control points for global orthorectification of GF-3," *Acta Geod. Cartogr. Sin.*, vol. 52, no. 11, pp. 1929–1940, 2023.

Qian Cheng received the master's degree in surveying and mapping science and technology from the School of Geomatics, Liaoning Technical University, Fuxin, China, in 2020. He is currently working toward the Ph.D. degree in photogrammetry and remote sensing with the School of Remote Sensing and Information Engineering, Wuhan University, Wuhan, China.

His main research interests include geometry processing of spaceborne synthetic aperture radar and 3-D reconstruction.
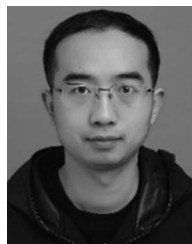
Taoyang Wang received the B.E. and Ph.D. degrees in photogrammetry and remote sensing from the School of Remote Sensing and Information Engineering, Wuhan University, Wuhan, China, in 2007 and 2012, respectively.

His doctoral dissertation concerned the block adjustment of high-resolution satellite remote sensing imagery. Since 2014, he has been working with the School of Remote Sensing and Information Engineering, Wuhan University, where he became an Associate Research Fellow in 2015. His research interests include space photogrammetry, geometry processing of spaceborne optical/SAR/InSAR imagery, target detection, and recognition based on satellite video.

Xin Li received the Master's degree in surveying and mapping engineering in 2020 from the Wuhan University, Wuhan, China, where he is currently working toward the Ph.D. degree in photogrammetry and remote sensing with the State Key Laboratory of Information Engineering in Surveying, Mapping and Remote Sensing.

His main research interests include geometry processing of spaceborne synthetic aperture radar and deep learning in remote sensing.

Yongcheng Wan received the B.E. degree in remote sensing in 2023 from the School of Remote Sensing and Information Engineering, Wuhan University, Wuhan, China, where he is working toward the Master's degree in photogrammetry and remote sensing with the School of Remote Sensing and Information Engineering.

His main research interests include geometry processing of spaceborne synthetic aperture radar and geometric correction.

Maoqiang Jing received the B.E. degree in electronic and information engineering and the Master's degree in information and communication engineering from the University of Electronic Science and Technology of China, Chengdu, China, in 2016 and 2019, respectively, and the Ph.D. degree in photogrammetry and remote sensing from the State Key Laboratory of Information Engineering in Surveying, Mapping and Remote Sensing, Wuhan University, Wuhan, China, in 2022.